Supporting Information

for *Small*, DOI: 10.1002/smll.201905903

In Situ Intercalation of Bismuth into 3D Reduced Graphene Oxide Scaffolds for High Capacity and Long Cycle-Life Energy Storage

Mengying Wang, Songlin Xie, Chengqiang Tang, Xin Fang, Meng Liao, Lie Wang, Yang Zhao, Yunzhou Wen, Lei Ye, Bingjie Wang, and Huisheng Peng**

Supporting Information

In situ intercalation of bismuth into three-dimensional reduced graphene oxide scaffolds for high capacity and long cycle-life energy storage

Mengying Wang[†]*, Songlin Xie*[†]*, Chengqiang Tang, Xin Fang, Meng Liao,Lie Wang, Yang Zhao, Yunzhou Wen, Lei Ye, Bingjie Wang* and Huisheng Peng**

Laboratory of Advanced Materials, State Key Laboratory of Molecular Engineering of Polymers, and Department of Macromolecular Science, Fudan University, Shanghai 200438, China.

[†]*These authors contributed equally to this work.*

**E-mail: wangbingjie@fudan.edu.cn; penghs@fudan.edu.cn.*

1. Electrode resistances in the transmission line model (TLM)

For non-faradaic (equivalent circuit as shown in Figure S8a) and faradaic processes, the overall impedance is expressed as Equations 1 and 2.

$$Z_{\text{nonfaradaic}} = \sqrt{\frac{R_{ion,L}}{jwC_{dl,A} \cdot 2\pi r}} \coth \sqrt{R_{ion,L} \cdot jwC_{dl,A} \cdot 2\pi r} L \qquad (1)$$

$$Z_{\text{faradaic}} = \sqrt{\frac{R_{ion,L} \cdot R_{ct,A}}{(1 + jwR_{ct,A} \cdot C_{dl,A}) \cdot 2\pi r}} \coth \sqrt{\frac{R_{ion,L} \cdot (1 + jwR_{ct,A} \cdot C_{dl,A}) \cdot 2\pi r}{R_{ct,A}}} L \qquad (2)$$

Where $R_{ion,L}$ is the ionic resistance per unit pore length and R_{ion} is the ionic resistance in the electrolyte-filled pores inside the porous electrode. R_{ion} can be thus expressed in Equations 3 and 4. In addition, R_{ct} is expressed in Equation 5.

$$R_{ion} = R_{ion,L} \times \frac{L}{n} \qquad (3)$$

$$R_{ion,L} = \frac{\rho}{\pi r^2} \qquad (4)$$

$$R_{ct} = \frac{R_{ct,A}}{2\pi r L} \qquad (5)$$

The limitation values of the real (Z'_{ω}) as $w \rightarrow 0$ in nonfaradaic and faradaic processes are shown by Equations 6 and 7, respectively.

$$Z'_{\text{nonfaradaic},\omega \rightarrow 0} = \frac{R_{ion}}{3} \qquad (6)$$

$$Z'_{\text{faradaic},\omega \rightarrow 0} = \frac{R_{ion}}{3} + R_{ct} \qquad (7)$$

The limitation values of the imaginary part (Z''_{ω}) as $\omega \rightarrow 0$ in nonfaradaic and faradaic processes are shown by Equations 8 and 9, respectively.

$$Z''_{\text{nonfaradaic},\omega\to 0}=\frac{1}{\omega C_{\text{dl}}} \qquad (8)$$

$$Z''_{\text{faradaic},\omega\to 0}=0 \qquad (9)$$

2. Capacity calculation

(1) Single electrode

Areal capacity of the single electrode was calculated from galvanostatic discharge profile based on the following equation,

$$C_A=\frac{\int_0^{\Delta t} I\times dt}{S} \qquad (10)$$

where C_A (mAh·cm^{-2}) is the areal capacity, I (mA) is the constant discharging current, Δt (h) is the discharging time, and S (cm^2) is the area of the electrode (1 cm^2).

Specific capacity of the Bi electrode was calculated from galvanostatic discharge profile based on the following equation,

$$Cs=\frac{\int_0^{\Delta t} I\times dt}{m} \qquad (11)$$

where Cs (mAh g^{-1}) is the specific capacity, I (mA) is the constant discharging current, Δt (h) is the discharging time, and m (g) is the mass of Bi (excluding the rGO content).

(2) Ni//Bi full battery

The areal cell capacity ($C_{\text{cell-A}}$) was calculated from galvanostatic discharge profiles based on Equation 10. Here S is the area of the cell (1 cm^2).

Specific capacity ($C_{\text{cell-s}}$) of the cell was calculated from galvanostatic discharge profile based on Equation 11. Here m (g) is the mass of Bi (excluding the rGO content).

Volume energy density (E) and volume power density (P) of the cell were obtained from the following equations,

$$E = \frac{C_{\text{cell-A}} \times V}{h} \qquad (12)$$

$$P = \frac{C_{\text{cell-A}} \times V}{1000 \times h \times \Delta t} \qquad (13)$$

where E (mWh cm^{-3}) is the areal energy density, $C_{\text{cell-A}}$ is the areal cell capacity, V (V) is the average discharge voltage, and h (cm) is the height of the cell. P (W cm^{-3}) is the volume power density and Δt (h) is the discharging time.

3. XAES characterization and data processing

Bi K-edge absorption spectra were performed on the 1W1B beamline of the Beijing Synchrotron Radiation Facility, China. The Si monochromator energy was calibrated with Pt foil rising edge energy. The spectra were obtained from 13.2 to 14.2 keV for Bi L_3-edge at 0.5 eV steps at the near edge. For the standard samples, they were all prepared by being uniformly placed on 3M tape.

All XANES data were processed by *Athena* software included in *Demeter* software package[1]. The absorption edge energy E_0 of Pt foil was aligned to 11564 eV. E_0 of Pt foil was assigned by the first maximum of first-derivative XANES spectrum. All data of Bi were aligned according to the standard Pt foil. The near edge linear combination fits were carried out by LCF fits program embedded in *Athena* software using Bi and Bi_2O_3 as standard samples.

The simulation of EXAFS spectra of rGO/Bi samples were carried out by the FEFF6 codes embedded in the *Artemis* software. The crystallographic information file (CIF) of Bi_2O_3 were used as models to calculate raw scattering paths. The experimental spectra were fitted by raw scattering paths at a k-range of 3 to 12 Å^{-1}.

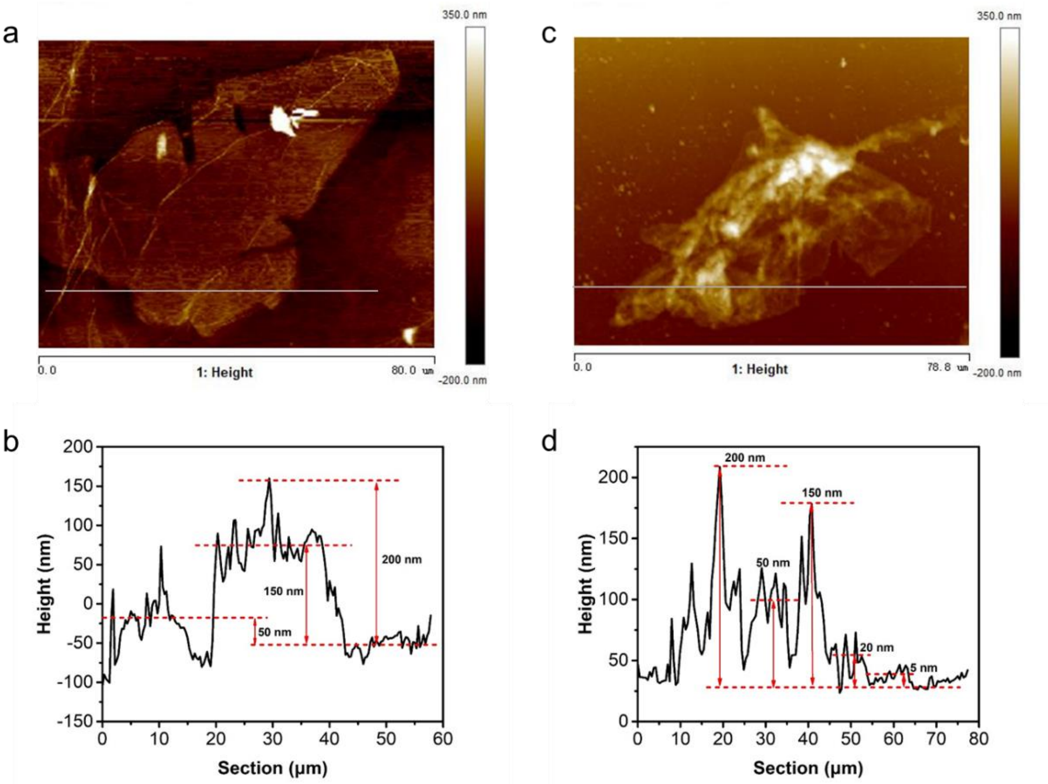

Figure S1. Topographic image (**a**, **b**) and height profile (**c**, **d**) of GO and GO/Bi^{3+} obtained from the solution.

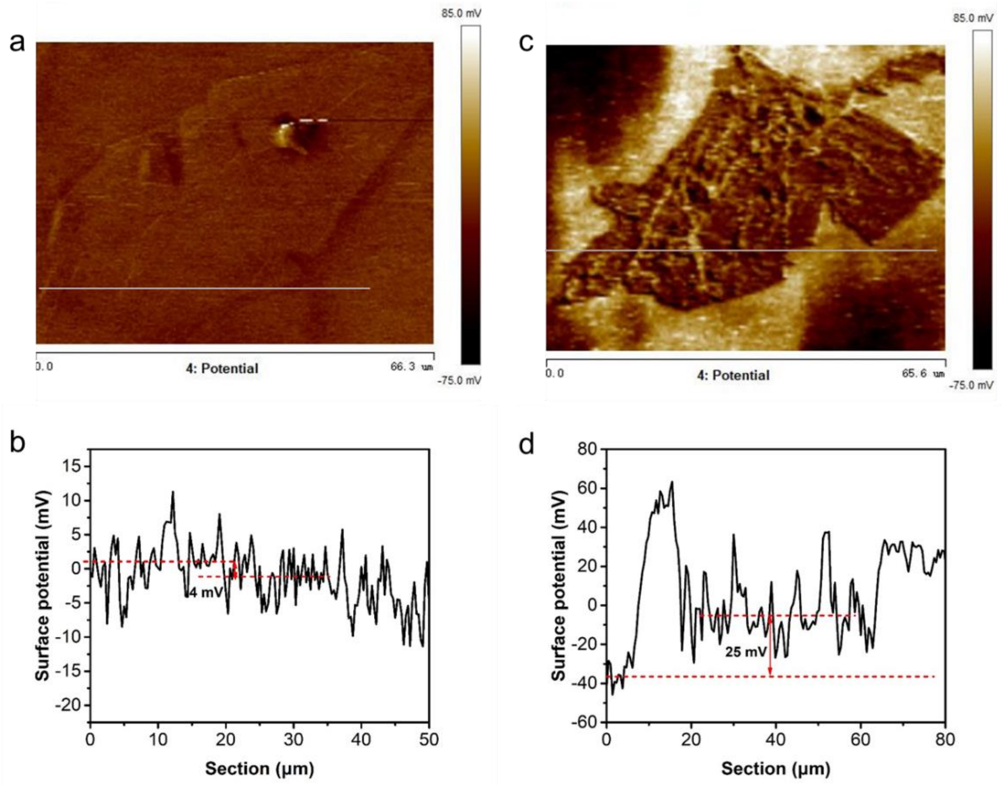

Figure S2. Topographic image (**a**, **b**) and surface potential graph (**c**, **d**) of GO and GO/Bi^{3+} obtained from the solution.

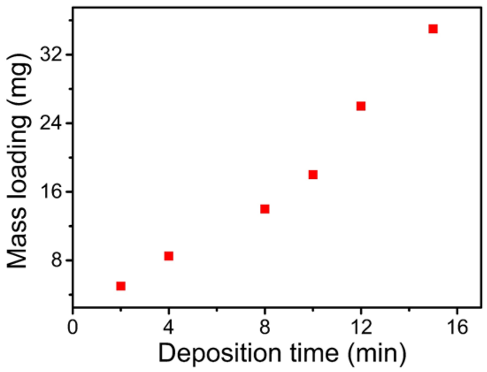

Figure S3. Dependence of mass load of rGO/Bi hybrid on deposition time.

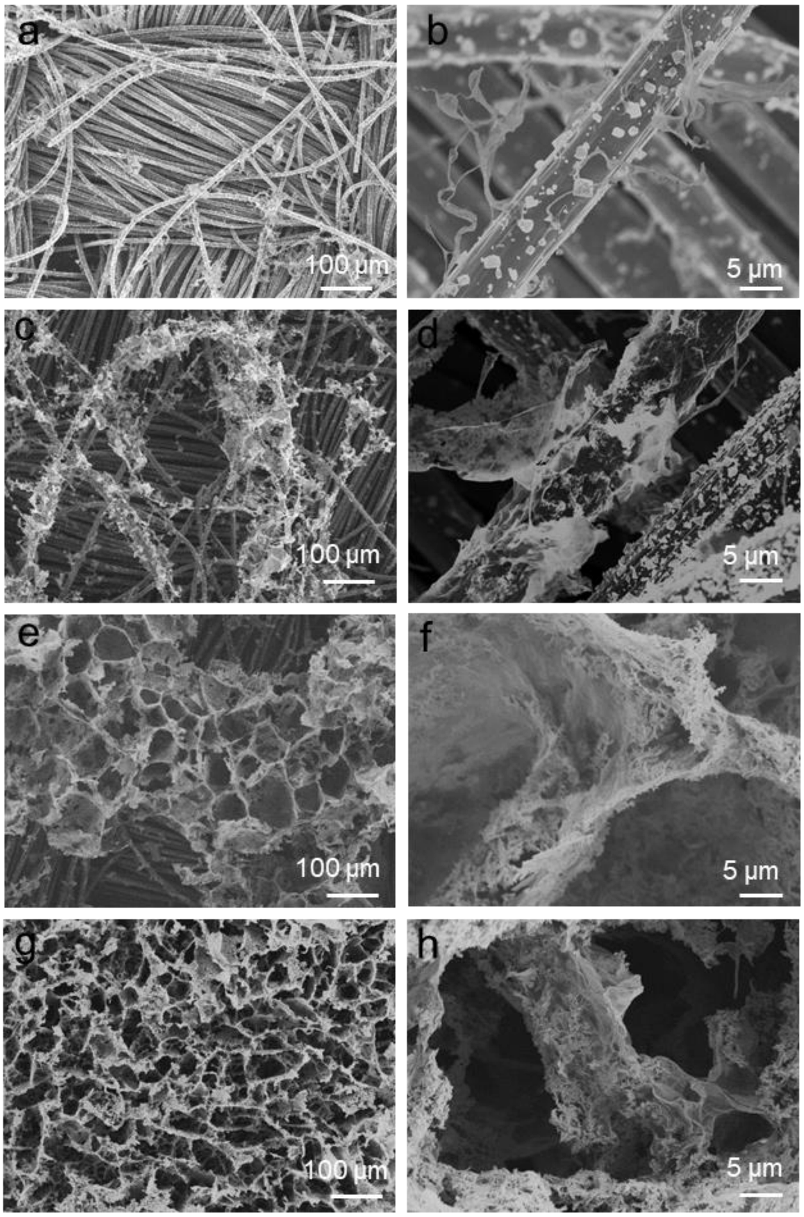

Figure S4. SEM images at low (left column) and high (right column) magnifications for the rGO/Bi hybrid after deposition of 5s (**a**, **b**), 13s (**c**, **d**), 40s (**e**, **f**) and 150s (**g**, **h**).

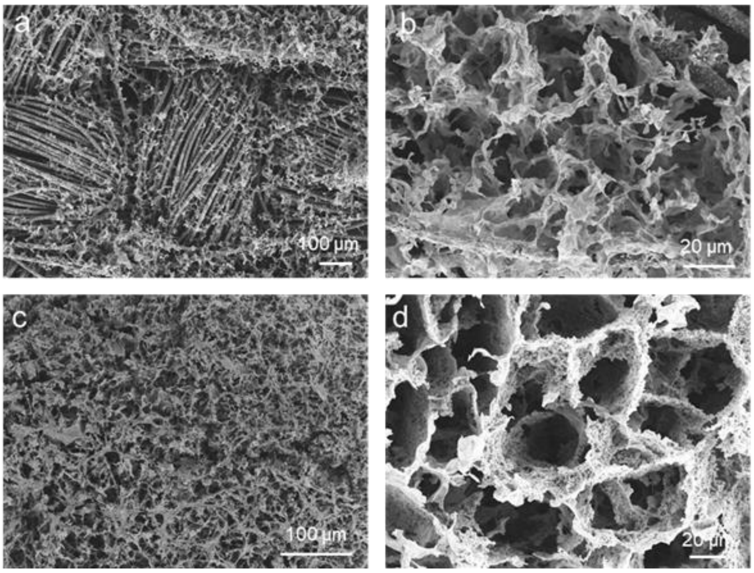

Figure S5. Scanning electron microscopy (SEM) images at low (left column) and high (right column) magnifications for the rGO/Bi hybrid after deposition of 20 s (a, b) and 260 s (c, d).

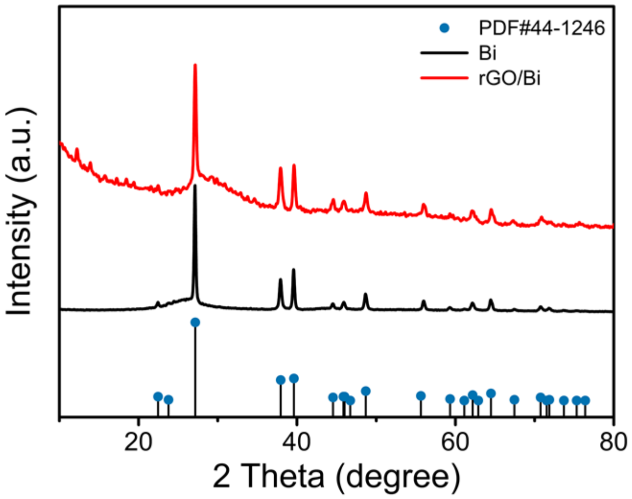

Figure S6. XRD spectra of Bi and rGO/Bi hybrid.

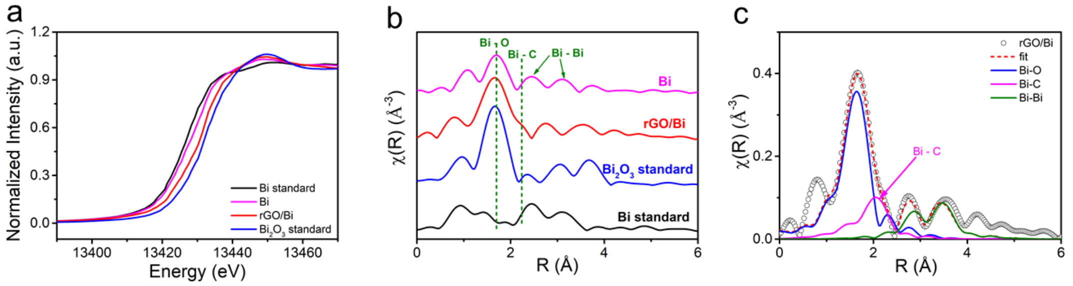

Figure S7. XANES (**a**) and EXAFS (**b**) spectra of Bi and rGO/Bi hybrid. Here Bi was prepared from the same electrodepositing solution without GO. (**c**) EXAFS spectra of the rGO/Bi hybrid and its fitted curves.

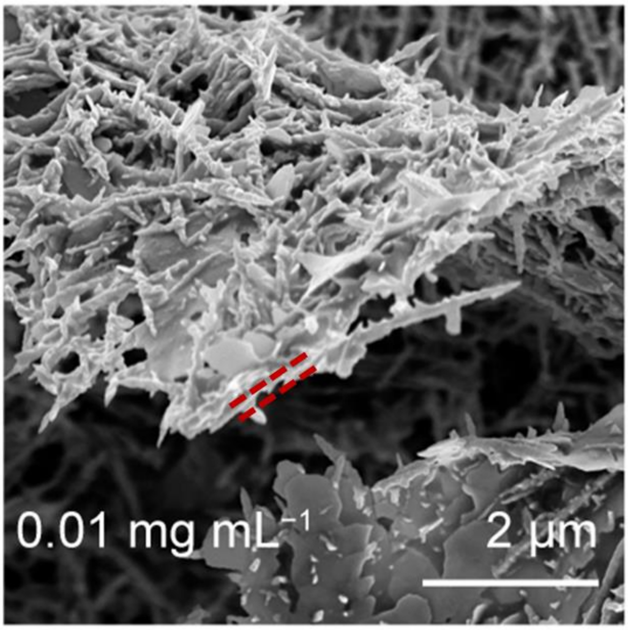

Figure S8. SEM image of rGO/Bi hybrid prepared with 0.01 mg mL^{-1} GO in the electroplating solution.

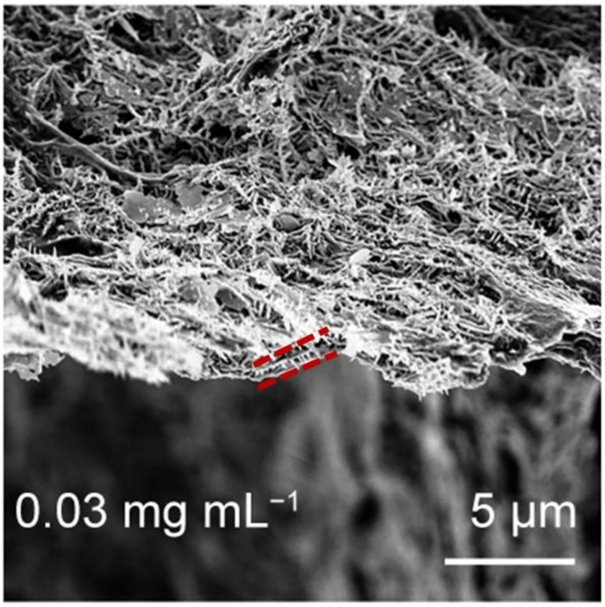

Figure S9. SEM image of rGO/Bi hybrid prepared with 0.03 mg mL^{-1} GO in the electroplating solution.

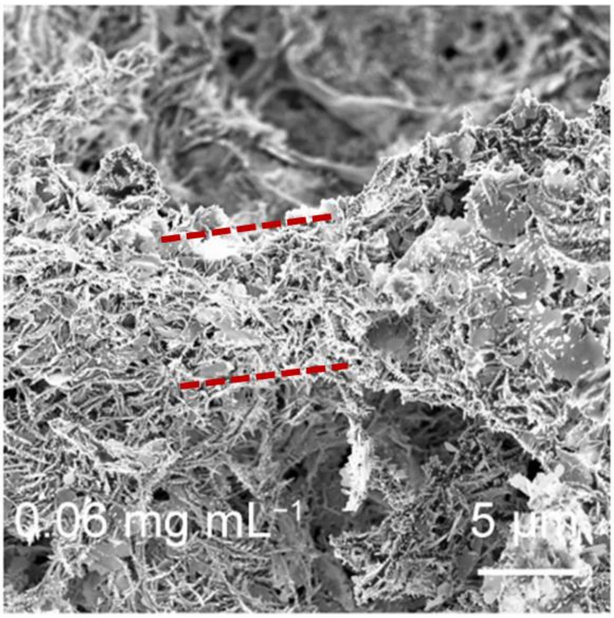

Figure S10. SEM image of rGO/Bi hybrid prepared with 0.06 mg mL^{-1} GO in the electroplating solution.

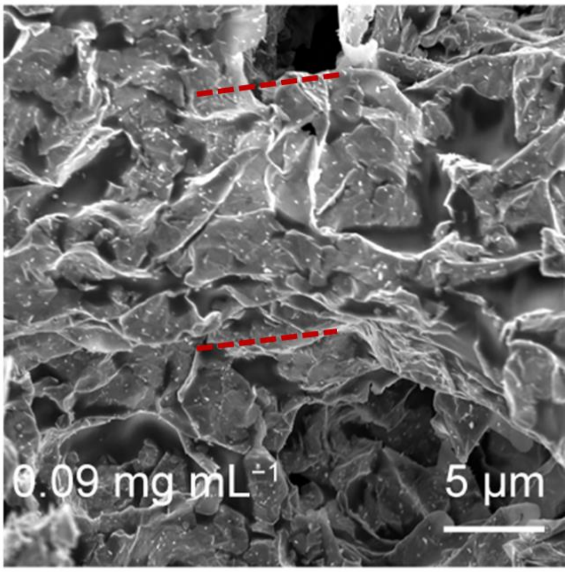

Figure S11. SEM image of rGO/Bi hybrid prepared with 0.09 mg mL^{-1} GO in the electroplating solution.

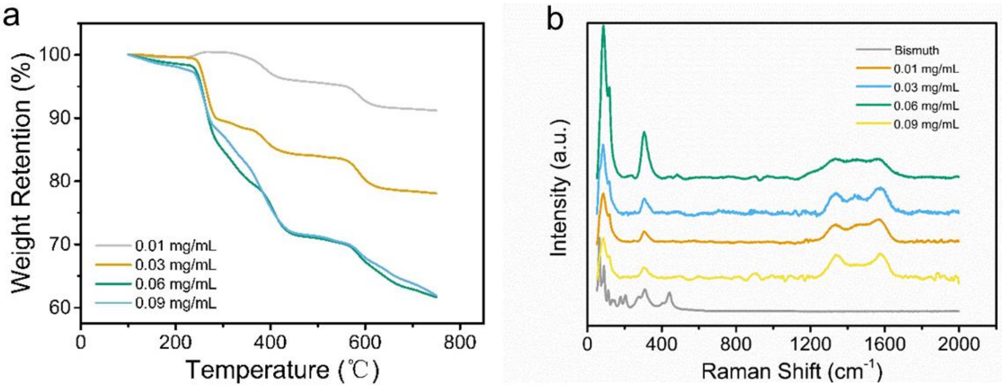

Figure S12. Thermogravimetric analysis (**a**) and Raman (**b**) spectra of rGO/Bi hybrids obtained from the deposition solutions with increasing GO concentrations.

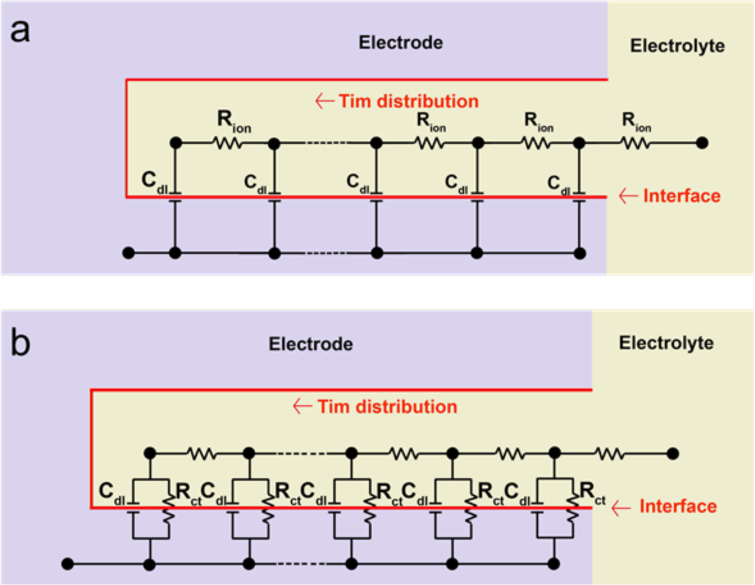

Figure S13. Equivalent circuit models of porous electrodes. (**a**) Non-faradaic process at state of charge (SOC) of 0% for porous electrodes. (**b**) Faradaic process at SOC higher than 0%. R_{sol} is the ohmic resistance originated from the electrolyte; R_{ion} is the ionic resistance in the electrolyte-filled porous electrode; C_{dl} and R_{ct} are the double layer capacitance and charge-transfer resistance, respectively.

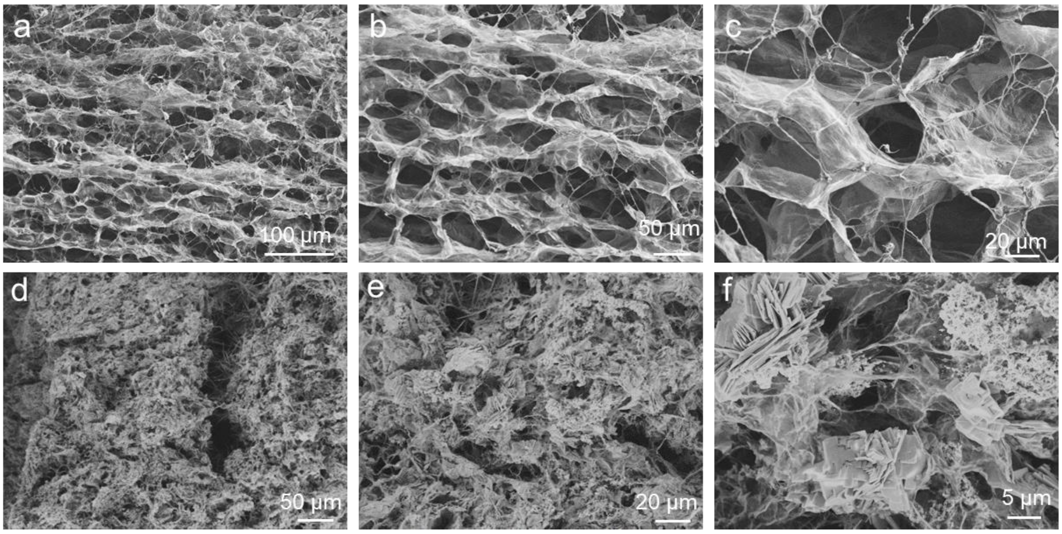

Figure S14. SEM images of rGO (**a-c**) and rGO+Bi hybrid (**d-f**) with increasing magnifications.

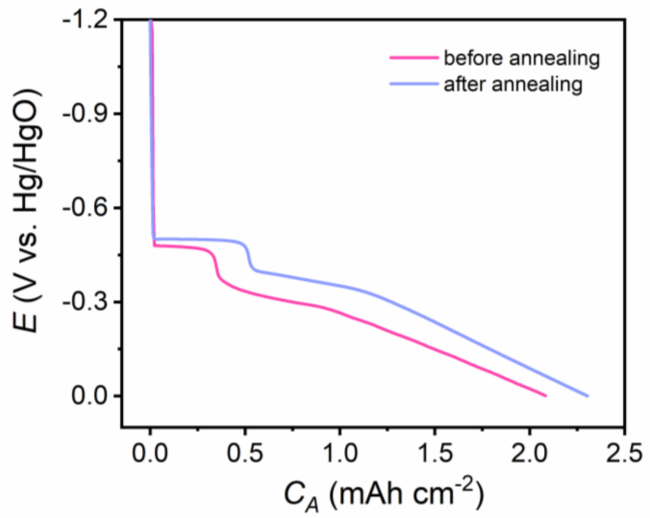

Figure S15. Galvanostatic discharge curves of rGO/Bi electrodes before and after annealing treatment at 20 mA·cm^{-2} with the load density of 30 mg·cm^{-2}.

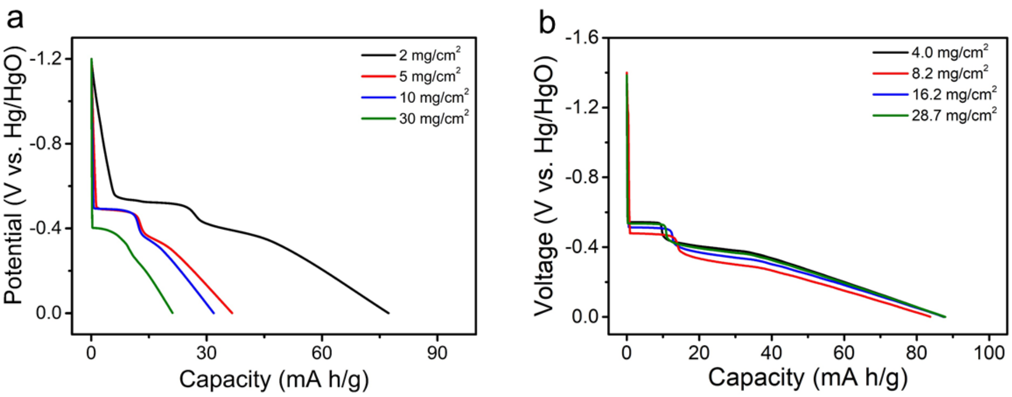

Figure S16. Galvanostatic discharge profiles of the rGO+Bi (**a**) and rGO/Bi (**b**) electrodes with increasing load densities of active material at 4 mA·cm^{-2}.

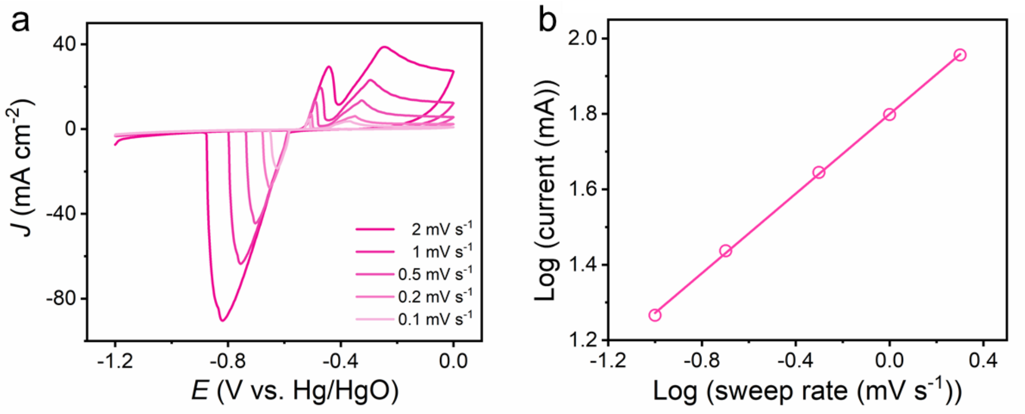

Figure S17. **a**) CV curves of the rGO/Bi electrode at increasing scan rates. **b**) Determination of the *b* value (i.e., 0.53) according to the relationship between sweep rate and current of the rGO/Bi electrode.

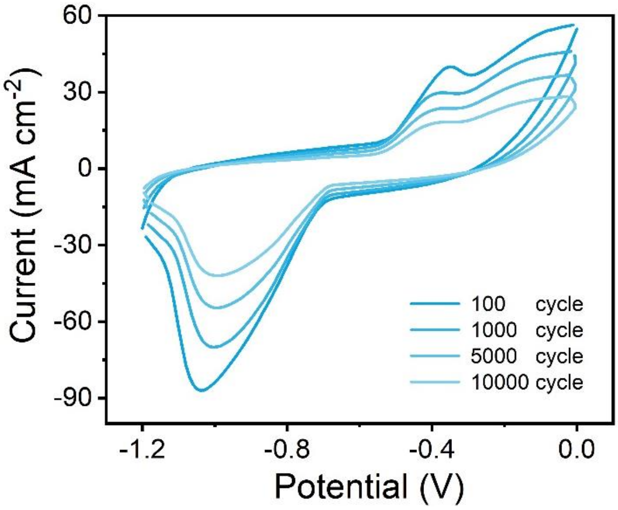

Figure S18. CV curves of rGO+Bi hybrid electrode after different cycles at 100 mV·s^{-1}.

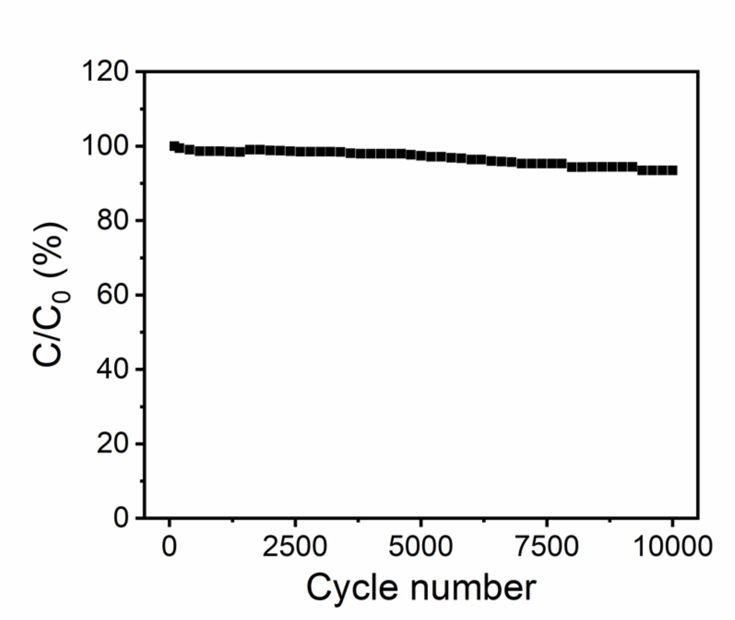

Figure S19. Cyclic stability of the rGO/Bi electrode at 50 mA·cm^{-2}.

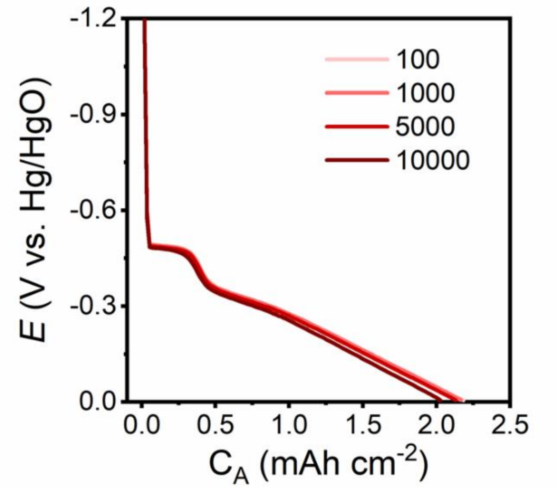

Figure S20. Galvanostatic charge and discharge curves of the rGO/Bi electrode after different cycles.

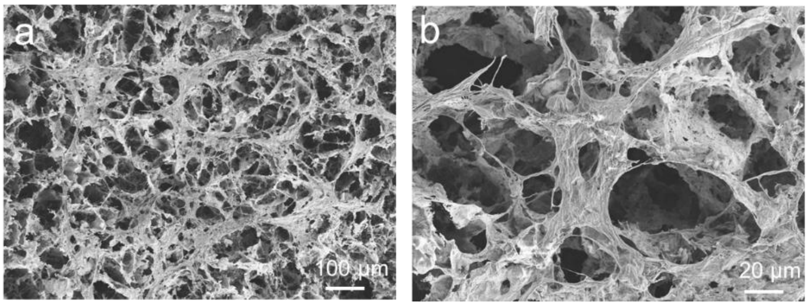

Figure S21. SEM images of the rGO/Bi electrode after 1,000 cycles at low (**a**) and high (**b**) magnifications.

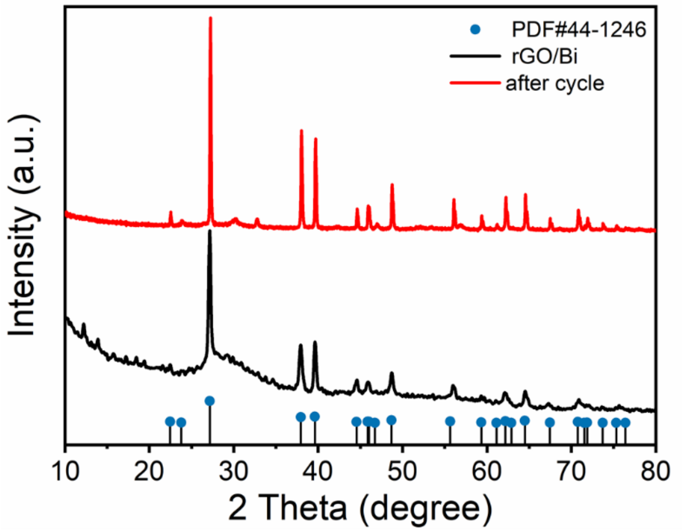

Figure S22. XRD patterns of the rGO/Bi electrode after 1,000 cycles.

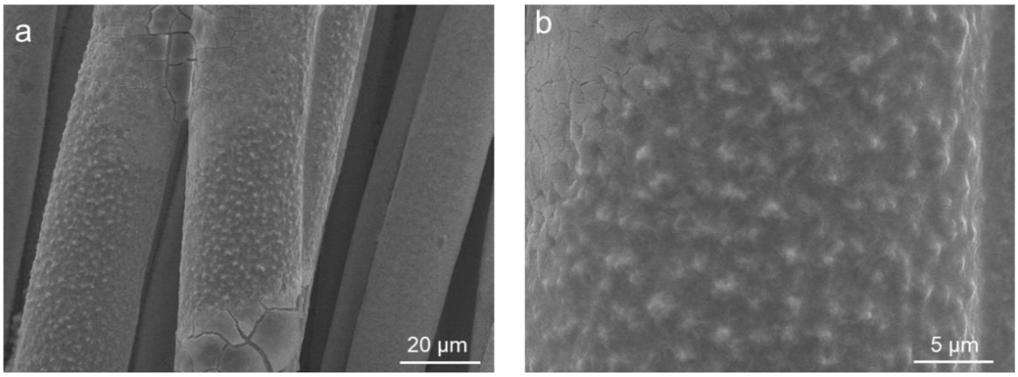

Figure S23. SEM images of Ni/NiO electrode at low (**a**) and high (**b**) magnifications.

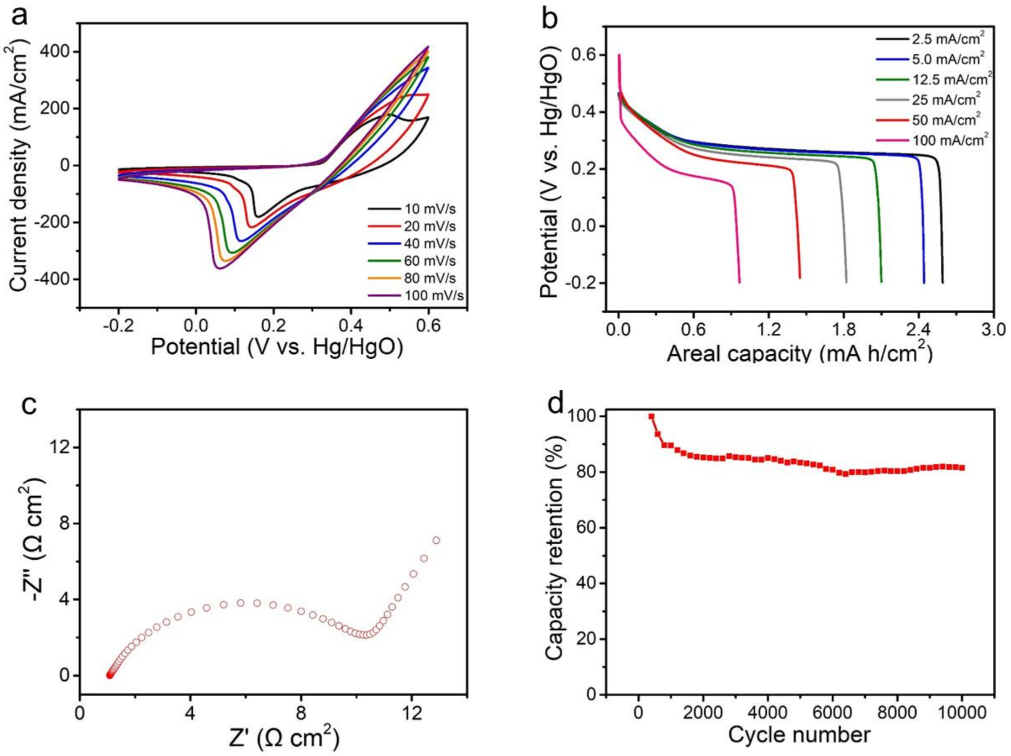

Figure S24. (**a**) CV curves of the Ni/NiO electrode at increasing scan rates. (**b**) Galvanostatic discharge curves of the Ni/NiO electrode at increasing current densities. (**c**) Nyquist plots. (**d**) Cycling performance of the Ni/NiO electrode.

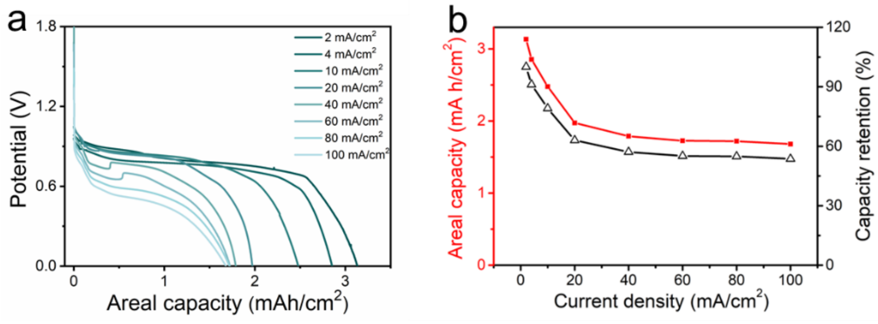

Figure S25. **a**) Galvanostatic discharge profiles of the Ni-Bi full battery at increasing current densities. **b**) Areal capacity and capacity retention of the Ni-Bi full battery.

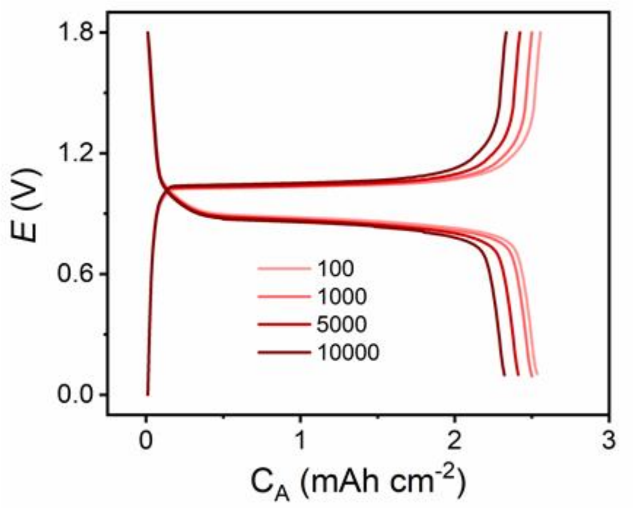

Figure S26. Galvanostatic charge and discharge curves of the Ni-Bi full battery after 100, 1,000, 5,000 and 10,000 cycles.

Table S1. Areal capacities and load densities for rGO/Bi hybrid electrodes compared to the other Bi electrodes and anodes for Ni-based batteries.

Electrode	Load density (mg·cm^{-2})	Retention	Rate capacity (mAh·cm^{-2}) @(mA·cm^{-2})		Ref.
rGO/Bi	39.8	83%, 100 mV·s^{-1}, 50,000 cycles	3.5@(2)	2.3@(100)	this work
Bi_2O_3	5	74.5%, 2 A·g^{-1}, 200 cycles	0.6@(5)	--	[2]
Bi	0.665	96%, 10,000 cycles	0.064@(3)	0.060@(30)	[3]
CNF/ Bi_2O_3	9	--	0.348@(3)	0.199@(15)	[4]
P/Bi/C	12.9	74.5%, 40 mA·cm^{-2}, 5,000 cycles	1.79@(4)	0.78@(120)	[5]
CF/Fe_3O_4	2	83.4%, 1,000 cycles	0.41@(5)	0.3@(80)	[6]
CNT/Fe_2O_3	0.6	96%, 10 mV·s^{-1}, 1,000 cycles	0.17@(0.6)	0.06@(2.4)	[7]
G/FeO_x	0.7	80%, 40 mV·s^{-1}, 300 cycles	0.68@(0.5)	0.17@ (4)	[8]

Table S2. Comparison of energy storage performance of the current Ni-Bi full battery and the other energy storage systems.

Battery	Load density of anode material ($mg\cdot cm^{-2}$)	Energy density ($mWh\cdot cm^{-3}$)	Power density ($W\cdot cm^{-3}$)	Ref.
Ni/NiO//rGO/Bi	39.8	16.54	1.00	This work
		31.08	0.02	
Ni//Zn	0.6	10.67	0.014	[9]
Ni//Bi	11.3	16.9	0.038	[5]
Ni//Fe	2	5.2	0.065	[6]
Zn//MnO_2	3.6	6.4	0.466	[10]
MnO_2//Bi_2O_3 ASC	9	1.25	0.375	[4]

Table S3. Comparison of cyclic stability of Ni-Bi battery and other energy storage systems.

Battery	Cycle number	Capacity retention (%)	Ref.
Ni/NiO//rGO/Bi	10,000	91	This work
$Ni(OH)_2$@graphene//Bi_2O_3@graphene	200	60	[11]
$NiCo_2O_4$//Bi	1,000	89	[3]
$Ni(OH)_2//(BiO)_4CO_3(OH)_2$	80	77	[12]
$Ni(OH)_2//Fe_2O_3$	2,000	78	[7]
$MnO_2//Bi_2O_3$ ASC	4,000	85	[4]
$LiMn_2O_4//LiTi_2(PO_4)_3$	200	82	[13]
CuHCF/MnHCMn	1,000	95	[14]
Sodium-ion battery: $Na_{0.66}[Mn_{0.66}Ti_{0.34}]O_2//NaTi_2(PO_4)_3$	1,200	92.7	[15]
$Zn//Co_3O_4$	2,000	80	[16]
Zn $//Zn_{0.25}V_2O_5$	1,000	80	[17]
$Zn//MnO_2$	5,000	92	[18]
NiO//ZnO	2,500	73	[9]

References of the Supporting Information

[1] B. Ravel, M. Newville, *J. Synchrotron Radiat.* **2005**, *12*, 537.

[2] W. Zuo, W. Zhu, D. Zhao, Y. Sun, Y. Li, J. Liu, X. W. D. Lou, *Energy Environ. Sci.* **2016**, *9*, 2881.

[3] Y. Zeng, Z. Lin, Y. Meng, Y. Wang, M. Yu, X. Lu, Y. Tong, *Adv. Mater.* **2016**, *28*, 9188.

[4] H. Xu, X. Hu, H. Yang, Y. Sun, C. Hu, Y. Huang, *Adv. Energy Mater.* **2015**, *5*, 1401882.

[5] Y. Zeng, Z. Lin, Z. Wang, M. Wu, Y. Tong, X. Lu, *Adv. Mater.* **2018**, *30*, 1707290.

[6] C. Guan, W. Zhao, Y. Hu, Q. Ke, X. Li, H. Zhang, J. Wang, *Adv. Energy Mater.* **2016**, *6*, 1601034.

[7] J. Liu, M. Chen, L. Zhang, J. Jiang, J. Yan, Y. Huang, J. Lin, H. J. Fan, Z. X. Shen, *Nano Lett.* **2014**, *14*, 7180.

[8] H. Wang, Y. Liang, M. Gong, Y. Li, W. Chang, T. Mefford, J. Zhou, J. Wang, T. Regier, F. Wei, H. Dai, *Nat. Commun.* **2012**, *3*, 917.

[9] J. Liu, C. Guan, C. Zhou, Z. Fan, Q. Ke, G. Zhang, C. Liu, J. Wang, *Adv. Mater.* **2016**, *28*, 8732.

[10] Y. Zeng, X. Zhang, Y. Meng, M. Yu, J. Yi, Y. Wu, X. Lu, Y. Tong, *Adv. Mater.* **2017**, *29*, 1700274.

[11] J. Sun, J. Wang, Z. Li, L. Niu, W. Hong, S. Yang, *J. Power Sources* **2015**, *274*, 1070.

[12] J. Sun, Z. Li, J. Wang, W. Hong, P. Gong, P. Wen, Z. Wang, S. Yang, *J. Alloys Compd.* **2015**, *643*, 231.

[13] J. Y. Luo, Y. Y. Xia, *Adv. Funct. Mater.* **2007**, *17*, 3877.

[14] A. Firouzi, R. Qiao, S. Motallebi, C. W. Valencia, H. S. Israel, M. Fujimoto, L. A. Wray, Y.-D. Chuang, W. Yang, C. D. Wessells, *Nat. Commun.* **2018**, *9*, 861.

[15] L. Suo, O. Borodin, Y. Wang, X. Rong, W. Sun, X. Fan, S. Xu, M. A. Schroeder, A. V. Cresce, F. Wang, C. Yang, Y.-S. Hu, K. Xu, C. Wang, *Adv. Energy Mater.* **2017**, *7*, 1701189.

[16] X. Wang, F. Wang, L. Wang, M. Li, Y. Wang, B. Chen, Y. Zhu, L. Fu, L. Zha, L. Zhang, Y. Wu, W. Huang, *Adv. Mater.* **2016**, *28*, 4904.

[17] D. Kundu, B. D. Adams, V. Duffort, S. H. Vajargah, L. F. Nazar, *Nat. Energy* **2016**, *1*, 16119.

[18] H. Pan, Y. Shao, P. Yan, Y. Cheng, K. S. Han, Z. Nie, C. Wang, J. Yang, X. Li, P. Bhattacharya, K. T. Mueller, J. Liu, *Nat. Energy* **2016**, *1*, 16039.